

See discussions, stats, and author profiles for this publication at:
<https://www.researchgate.net/publication/225565074>

Impact of mechanical loading on the corrosion of steel reinforcement in concrete structures

Article *in* Materials and Structures · July 2011

Impact Factor: 1.71 · DOI: 10.1617/s11527-010-9688-3

CITATIONS

5

READS

58

2 authors:



[Ayman Ababneh](#)

Jordan University of Science and Tech...

26 PUBLICATIONS 197 CITATIONS

[SEE PROFILE](#)



[Mashal Sheban](#)

Hadhramout University

6 PUBLICATIONS 58 CITATIONS

[SEE PROFILE](#)

Impact of mechanical loading on the corrosion of steel reinforcement in concrete structures

Ayman Ababneh · Mashal Sheban

Received: 11 January 2010 / Accepted: 5 November 2010 / Published online: 23 November 2010
© RILEM 2010

Abstract This paper presents results of an experimental investigation on the effect of mechanical loading on the corrosion of steel reinforcement in concrete. Reinforced concrete beams were cast, subjected to mechanical loadings and then exposed to corrosive environment. Successive drying and wetting cycles using 3% sodium chloride salt solution were used to accelerate the corrosion attack. Electrochemical techniques such as macrocell corrosion current, linear polarization resistance (LPR), corrosion potential (E_{corr}) and electrochemical impedance spectroscopic (EIS), were used to evaluate the corrosion behavior of the reinforcement. Also, chloride penetration profile and visual inspection of the beam rebars were obtained. The results shows that the pre-exposure mechanical load has no influence on the corrosion initiation or corrosion rate thereafter, unless it reaches to some limit where it develops connected cracks through which the chloride ions flow and depassivate the rebars. The load of 25% of

the ultimate capacity seems to be the critical load limit where some microcracks onset to be connected, facilitate the chloride ions flow, and initiate the rebar corrosion.

Keywords Loading · Corrosion · Steel · LPR · EIS · Concrete

1 Introduction

Corrosion of steel reinforcement is a major deterioration mechanism for concrete structures in cold, marine, and industrial environments. Corrosion damage accelerates the aging of highway bridges, concrete pavements, parking structures, waterfront structures, and water and wastewater treatment structures. This, in turn, shortens their remaining service life, requires expenditures for maintenance, repair or replacement, endangers the public safety, and damages the environment. Corrosion of steel reinforcement is a major deterioration mechanism for the infrastructure systems worldwide, and the coupling between the corrosion and mechanical loading induced damage is expected to accelerate the deterioration.

The interaction between applied mechanical loading or loading capacity and reinforcement corrosion were studied from two different views. It is well known that the corrosion of reinforcing rebars reduces the strength and stiffness, steel–concrete

A. Ababneh (✉)
Department of Civil Engineering, Jordan University
of Science and Technology, P.O. Box 3030,
Irbid 22110, Jordan
e-mail: anababneh@just.edu.jo

M. Sheban
Department of Civil Engineering, Hadramout University
of Science and Technology, P.O. Box 50512-50511,
Mukalla, Yemen
e-mail: msheban@hotmail.com

bond strength and the cross sectional area of the rebar. Therefore, a reduction in load carrying capacity, resistance to excessive deformation, and resistance to cracking clearly result from steel corrosion [1–6]. On the other hand, in studies of the impact of loading and cracking on the corrosion process of reinforced concrete structures, researchers have observed contradictory results. Benture et al. [7] and Li [8] showed that the increase of the crack width accelerates the time required to initiate the steel corrosion, but it has no significant effect on the corrosion rate thereafter. Jacobsen et al. [9] and Francois et al. [10] showed that the development of reinforcement corrosion was not influenced by crack width (up to 0.5 mm). Castel et al. [11] and Francois and Maso [12] found that the damage in the tensile zone increase the carbonation and chloride penetration, but the penetration of carbonation was less than 20 mm after 13 years of loading and whenever the crack opening, the penetration of harmful materials locally occurs. However, Yoon et al. [13] showed that the loading level and loading-induced cracks have significant effects on both corrosion initiation and the rate of corrosion propagation. Also, Kondratova et al. [14] noticed that pre-cracking increased the corrosion rate. The effect of mechanical loading and damage on propagation of reinforcement corrosion needs more studies to overcome this contradiction.

This research studied the impact of mechanical loading on corrosion of steel reinforcement in concrete structures. In this study, reinforced concrete beams were cast, and mechanical loadings were applied on the beams before exposed to the corrosive environment. The electrochemical techniques, i.e., macrocell corrosion current, linear polarization resistance (LPR), corrosion potential (E_{corr}) and electrochemical impedance spectroscopic (EIS), were used to evaluate the corrosion behavior of the reinforcement. The results show that the pre-exposure mechanical load has no influence on the corrosion initiation or corrosion rate thereafter, unless it reaches to some limit where it develops connected cracks through which the chloride ions flow and depassivate the rebar.

2 Experimental program

This section describes the laboratory experimental program which was used to evaluate the effect of

mechanical loading on corrosion of reinforcing rebar. The experimental procedure is similar to that outlined in ASTM G109_99a with some modifications. The material properties and mix proportion of concrete are presented. The dimensions of specimens and the exposure condition are discussed in the following subsections.

2.1 Materials

2.1.1 Aggregate

Crushed stone with a maximum size of 9 mm was used as coarse aggregates. The moisture content was 0.09% in accordance to ASTM C566. The bulk specific gravity (SSD) was 2.393, oven dry bulk specific gravity was 2.361, and the absorption capacity was 1.38% in accordance to ASTM C127. The dry rodded unit weight was 1594.6 kg/m³ in accordance to ASTM C29. The coarse aggregates met the standard gradation requirements as specified in ASTM C33.

Graded river sand was used as a fine aggregate with the fineness modulus equal to 2.54 in accordance to ASTM C136. The moisture content was 0.08% in accordance to ASTM C566. The bulk specific gravity (SSD) was 2.648, oven dry bulk specific gravity was 2.621, and the absorption capacity was 1.05% in accordance to ASTM C127. The fine aggregates met the standard gradation requirements as specified in ASTM C33.

2.1.2 Cement

Type I Portland cement was used for all mixes described in this study. The cement specific gravity was 3.2 and the compound composition is: C3S = 51% and C3A = 8%. Table 1 provides a summary of the cement composition as supplied by the manufacturer.

2.1.3 Steel rebars

The steel reinforcement was grade 60 deformed rebar (ASTM A615) with diameter 0.5 in (12.5 mm). The rebars were sand blasted to near white metal, cleaned by soaking in acetone and allowed to air dry according to ASTM G109_99a.



Table 1 Chemical composition of cement

Silica (SiO ₂)	20.60%
Alumina (Al ₂ O ₃)	5.00%
Iron oxide (Fe ₂ O ₃)	3.10%
Calcium oxide (CaO)	62.4%
Magnesium (MgO)	3.80%
Sulfur trioxide (SO ₃)	2.90%
Loss of ignition	1.3%
Insoluble residue	0.39%
Equivalent alkali (as Na ₂ O)	0.58%

2.2 Dimension of specimens

The specimen geometry used in this study is a concrete beam; the beam has dimension of 11 × 6 × 4.5 in (280 × 150 × 115 mm). Three rebars were installed in each beam. The bar length was 14 in (360 mm) drilled at one end to be fitted with a stainless steel screw. Both ends of each bar were taped with electroplater tape so that only an 8 in (200 mm) portion at the middle of the rebar was bare. Therefore, the exposure surface area was 12.57 in² (8107 mm²). Then neoprene tubes were placed on both ends, and the neoprene tubes were filled with epoxy from both sides.

2.3 Mixing proportion and curing condition

Normal concrete strength was used in this study with w/c ratio 0.55. The mixing proportion ratio was 1:0.55:2:2 of water:cement:fine aggregate:coarse aggregate (dry weight). The coarse aggregate and one third of the mixing water was added prior to starting the rotation of the mixer. Then, the mixer was started and the fine aggregate, cement, and water were added with the mixer running. The mixer was run for 3 min, followed by 3 min rest and then by 2 min of final mixing. The concrete was placed in the molds with three layers for beam specimens and two layers for the cylinders; each layer was rodded uniformly 25 times with the rounded end of the rod. To prevent evaporation of water from unhardened concrete, all samples were covered with plastic and maintained at standard room temperature. After 24 h, all specimens were demolded and cured for 28 days in a moist curing room where the relative humidity was higher than 95%. The mixing procedure was done according to ASTM C192, and the curing procedure was done

Table 2 Compressive strength results

Cementitious materials	7 days strength (MPa)	28 days strength (MPa)	200 days strength (MPa)	365 days strength (MPa)
Concrete	20	22	24	25

according to ASTM C511. The average compressive strength results of 3" × 6" cylinders are shown in Table 2.

2.4 Pre-exposure loading

Four different types of loading were applied on the beams before exposure to a corrosive environment. The first case was three-point bending load, and the loading was 50% of the ultimate capacity; for simplicity, it was named 3P50% loading. The second case was also three-point bending load, but the loading was 25% of the ultimate capacity; it was named 3P25% loading. The third case was four-point bending load, and the loading was 25% of the ultimate capacity; it was named 4P25% loading. The last case was no pre-exposure loading condition; it was named 0P00% loading. The locations of loads for these cases are shown in Fig. 1. These loading configurations initiated cracks on the top surface of the specimen where the corrosive agent was later applied. The ultimate section capacity of specimens was calculated based on the step-by-step method presented in Ersoy et al. [15].

2.5 Exposure test procedure

The corrosive environment was cycles of wetting and drying with sodium chloride solution to accelerate the corrosion process; these cycles were applied as follows. After removing the specimens from the curing room, the pre-exposure loading was applied. Then, the specimens were exposed to a constant humidity of 30 ± 5% relative humidity and at a constant room temperature inside a humidity controlled chamber. The period of the drying cycle was 2 weeks. Then, a Plexiglas dam was installed on the top surface, and an epoxy sealer was used to coat the four sides of the specimen and the top area outside the Plexiglas dam. This was done to ensure one-direction of solution intrusion. The ponding dam was filled with 1.5 inches height of 3% sodium chloride

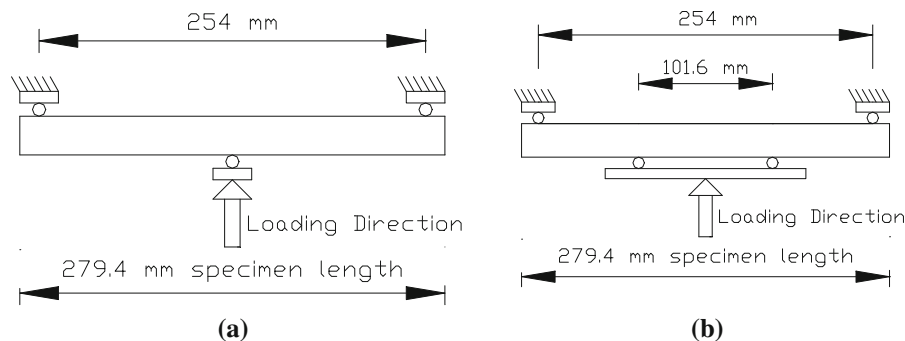


Fig. 1 Pre-exposure loading configurations. **a** Three-point loading and **b** four-point loading

solution (see Fig. 2). The period of wetting cycle was 2 weeks. During the wetting cycles, the ponding dam was covered to avoid solution evaporation. During the wetting and drying cycles, the top and bottom bars were connected by a 100 Ohm resistor to complete the macrocell circuit where the top bar worked as an anode and bottom bars as a cathode.

2.6 Experimental series

The effect of the pre-exposure loading was studied in this research. Two parameters were studied in this research: loading type, loading value. Four groups of different combinations of parameters were prepared, and each group had two replicate beams. Table 3 shows the group names and the experimental series.

3 Corrosion tests

The corrosion activity was measured at the middle of the wetting cycle according to ASTM G109_99a. Also, the corrosion potential, LPR and EIS tests were used to evaluate the corrosion resistance. All these tests were done once every 4 weeks (at the beginning of the second week of wetting cycles). The chloride penetration profiles of specimens also were measured. The application methods of those tests are presented in the following sections.

3.1 Macrocell current

When the concrete beam exposed to the chloride salt solution, the top rebar are typically ones to be exposed to the chloride ions and moisture. Thus, an electrochemical macrocell in concrete developed due

to the concentration gradients of moisture and chloride. As the macrocell is initiated, the top rebar becomes anodic than the bottom ones becomes cathodic, and a macrocell corrosion current flows between them. It is believed that these macrocells are the major driving force of reinforcement corrosion in concrete structures [16, 17].

The macrocell current as a function with time was monitored once every 4 weeks (at the beginning of the second week of wetting cycles). The macrocell current, I_j , calculated from the voltage, V_j , across the 100-Ohm resistor as follows:

$$I_j = \frac{V_j}{100} \quad (1)$$

The total integrated current is defined in ASTM G109_99a as follows:

$$TC_j = TC_{j-1} + [(t_j - t_{j-1}) * (I_j - I_{j-1})/2] \quad (2)$$

where TC is the total corrosion (Coulombs), t_j is the time (s) at which measurement of the macrocell current is carried out, and I_j is the macrocell current at time t_j .

3.2 Corrosion potential

The corrosion potential of each bar in the specimens was measured against the saturated calomel electrode (SCE) as a reference electrode which was placed in the dam containing the salt solution.

3.3 LPR studies

The LPR tests were carried out with three electrodes, i.e., reference, counter and working electrodes. The working electrode was the top steel rebar in the

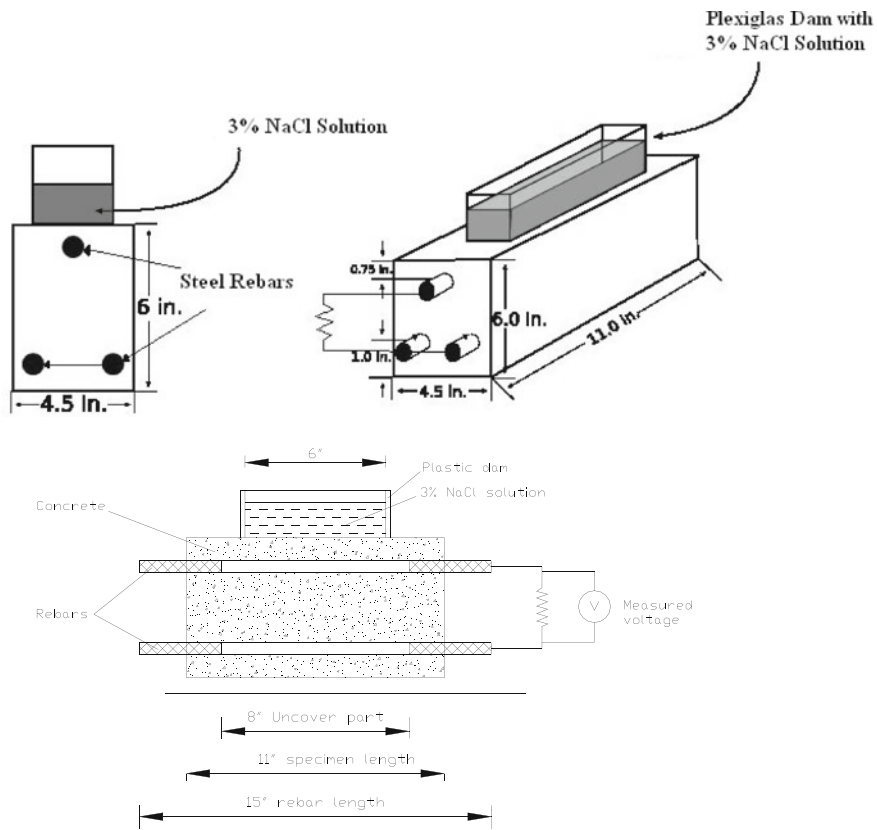


Fig. 2 Specimen details of exposure condition

Table 3 Experimental groups and series

Name	Pre-exposure loading
Series (1) loading type effect	
G7	3P25%
G8	4P25%
Series (2) loading value effect	
G6	3P50%
G7	3P25%
G9	0P00%

Symbols for specimen identification: *3P* three-point bending load, *4P* four-point bending load, *0P* no pre-exposure loading; 50, 25, 00% level of loading (% of ultimate capacity); *G#* group number

specimen. The counter electrode was the bottom steel rebar. The reference electrode was SCE placed in the dam containing the salt solution (see Fig. 3). The polarization scanned from a potential 15 mV more negative to 15 mV more positive of the corrosion potential of the top rebar, with a constant potential

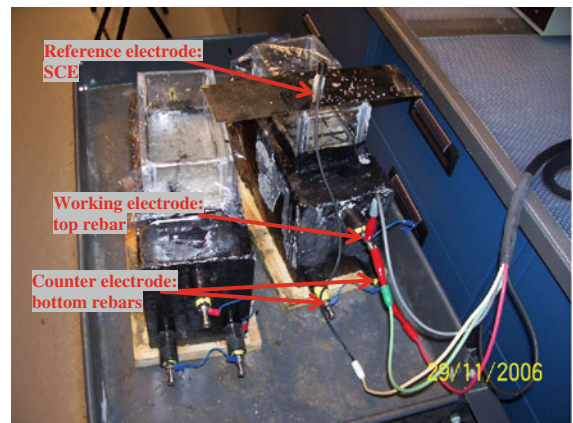


Fig. 3 Photo shows the connection configuration of LPR and EIS tests

scan rate of 0.125 mV/s. A Gamry potentiostat (model PCI4/300) was used to carry out the tests, and the obtained data were analyzed using the Gamry Echem Analyst software version 5.3.

3.4 Electrochemical impedance studies

The electrochemical A.C. impedance spectra (EIS) tests were carried out with the same configuration as LPR test. The measurements were recorded at the corrosion potential by applying a ± 10 mV sine wave in a frequency range from 100 kHz to 5 mHz (see Fig. 3). The obtained data were analyzed using the Gamry Echem Analyst software version 5.3.

3.5 The chloride penetration profiles

The chloride penetration profiles of concrete specimens were obtained using Rapid Chloride Test (RCT). RCT developed by Germann Instruments, Inc, and it is equivalent to AASHTO T-260 and ASTM C144. The RCT gives the percent of the total chloride content to the concrete weight. Concrete powder samples were collected from certain depth ranges by using a hammer drill. The top surface of specimens was cleaned from salt deposits by using a wire brush. Drilling started from the top surface which exposed to chloride penetration and extends at $\frac{1}{2}$ in (12.5 mm) depth increments. Six different location samples were collected in each concrete beam, and the powder from each two adjacent holes mix as one sample. A 1.5 g of each concrete powder was dissolved in an extraction solution and shaken 5 min, and then m-Volt reading was recorded by Chloride Ion-Selective electrode. Then the recorded mV-readings were converted to total chloride concentrations by using a calibration curve for the known standard calibration solutions (more details are given in [18]).

4 Results

The beams exposed to nine wetting/drying cycles and the results are averaged for each group. Each test result is presented separately in each following sections.

4.1 Macrocell current

The total macrocell current was calculated based on the voltage measured across the 100-Ohm resistor and using the Eqs. 1 and 2. Results are shown in Fig. 4. The three-point bending loaded with 50% of

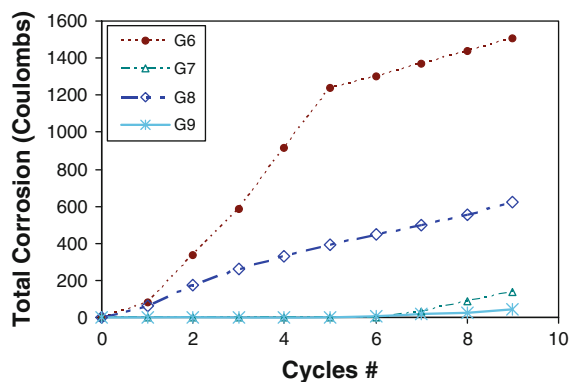


Fig. 4 Macrocell current results for groups G6–G9

the ultimate capacity (G6) suffered from high macrocell corrosion current compared to other loading conditions (G7–G9). In addition, the four-point bending (G8) showed higher current than three-point bending (G7) for the same loading level. The three-point bending loaded with 25% of the ultimate capacity group (G7) was similar to no pre-exposure loading (G9).

4.2 Corrosion potential results

The corrosion potential was monitored for all specimens. The average of group measurements is shown in Fig. 5. According to ASTM C876, if the half cell potential reading is more positive than -126 mV versus SCE, there is a lower than 10% probability that no reinforcing steel corrosion is occurring. If the potential reading is more negative than -276 mV versus SCE, it is assumed that a greater than 90% probability of reinforcing steel corrosion is occurring. If the potential reading is the range between -126

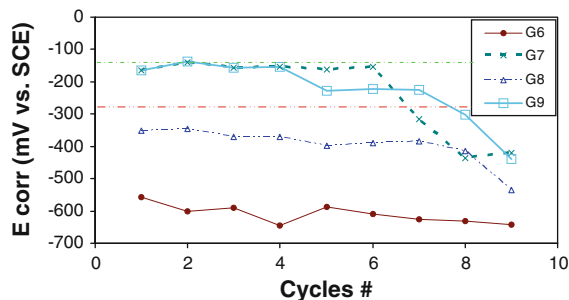


Fig. 5 Corrosion potential results for groups G6–G9. The two horizontal lines represent the ASTM C876 corrosion risk limits

and -276 mV versus SCE, it is assumed that the corrosion activity is uncertain.

Figure 5 shows the corrosion potential for the groups G6–G9. The matches between the corrosion potential of these curves with the macrocell corrosion current are very good. Both G7 and G9 are within uncertain corrosion activates as seen in Fig. 5 and their macrocell corrosion current readings were equal to zero, also their macrocell current curves begin to rise when their potential move to active zone. The G6 has more negative potential readings than the G9 which agrees with higher macrocell current shown in Fig. 4. In the same trend, G8 has more negative potential readings than both G7 and G9, and it has higher macrocell corrosion current.

4.3 LPR results

The polarization resistance, R_p , is calculated according to Jones [16], and the average values are shown in Fig. 6. The polarization resistance of G9 is improved with time due to the passive film formed around the rebar without any disturbance by ions chloride. Also, the resistance of G7 is better than G8 which is consistency with the macrocell current and corrosion potential results.

The corrosion current density, i_{corr} , and the corrosion rate, CR, were evaluated based on the polarization resistance. The value B , which depends on the Tafel slopes, must be account for the rebar materials and conditions (passive or active). It becomes more acceptable to use B values of 0.026 and 0.052 for steel in concrete in active and passive cases, respectively

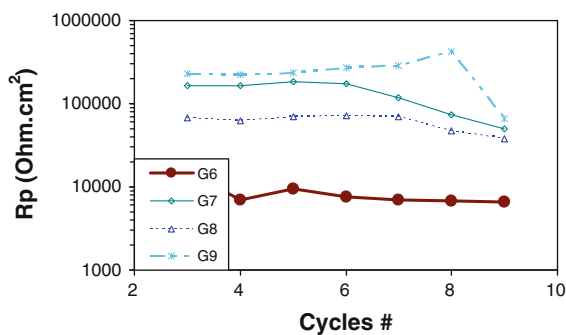


Fig. 6 Polarization resistance results from LPR test for groups G6–G9

[7, 16, 19, 20]. These values of B were used to calculate the corrosion current and corrosion rate.

Figure 7 shows the corrosion current density, i_{corr} , and the corrosion rate, CR. The G7 and G9 have very low corrosion rate as compared to G6. Also, G8 shows around 75% corrosion current lower than G6. Also, the corrosion current and potential trends matched with other works [21].

The calculated corrosion current and corrosion rate above were based on the LPR calculation method. This approach based on the B values which are approximately values and have an error of factor 2 [7, 16]. Also this approach considers the corrosion of the rebar as a uniform corrosion. This assumption was correct for the G7–G9 for the first eight cycles and before the pitting was started.

4.4 Electrochemical impedance (EIS) results

EIS data is generally analyzed in terms of an equivalent circuit model. The analyst tries to find a model whose impedance matches the measured data like Randles circuit shown in Fig. 8a. The R_s resistor represents the solution resistor and R_{ct} is the charge transfer resistor. The capacitance C_{dl} is related to the double layer that forms in electrochemical systems at the metal/solution interface.

Impedance spectra often become more complex to model by the Randles circuit, especially when a rebar has an organic coating or the corrosion products formed a layer on the rebar. In these cases, the impedance spectra with two time constants appear with two semicircles. Figure 8b illustrates equivalent circuit model for this behavior used by many researchers [22–27]. The equivalent circuit includes

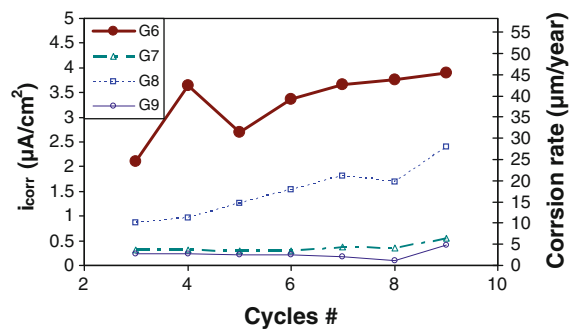


Fig. 7 Corrosion current and corrosion rate results from LPR tests for groups G6–G9

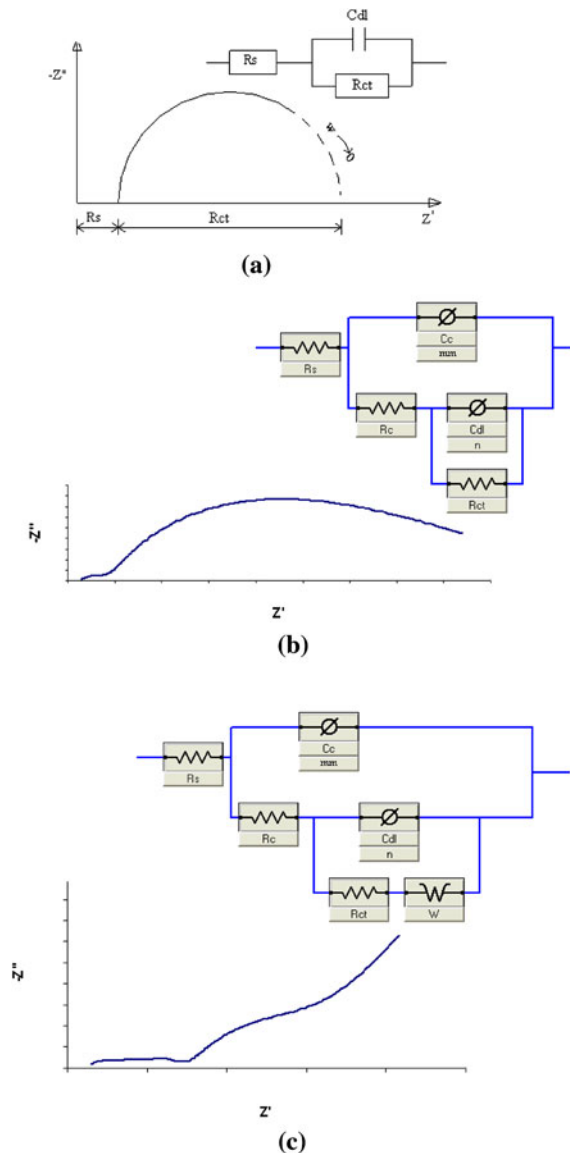


Fig. 8 Schematic diagram of Nyquist plots and associated equivalent circuits. **a** Nyquist plot and equivalent Randles circuit, **b** Nyquist plot and equivalent circuit with CPE elements and two time constants (double loops), and **c** Nyquist plot and equivalent circuit with two time constants and Warburg impedance (double loops with Warburg tail)

a coating capacitance (C_c) represented by a constant phase element (CPE). Also, the circuit includes a resistance R_c which represented the formation of ionically conducting paths across the coating between the electrolyte and substrate or the resistance of the formation of the corrosion products in cement pores around the rebar. The second loop of Nyquist

diagram accounted for the corrosion process at the coating substrate interface where C_{dl} is the double layer capacitance and R_{ct} is the charge transfer resistance (the corrosion resistance of the substrate). This equivalent circuit was named as double loops circuit in this study.

In some cases of control by diffusion (concentration polarization), a Warburg impedance effect appear in the EIS spectra (see Fig. 8c). In this case, an additional resistive element called a Warburg impedance must be added to the circuit. The Warburg impedance is evidenced at low frequencies on the Nyquist diagram by a straight line superimposed on the second circuit [16, 28, 29]. Figure 8c shows the circuit that can be used to model the EIS spectra with diffusion process. This equivalent circuit was named as double loops with Warburg tail circuit in this study.

The electrochemical A.C. impedances of all beams in this study have two time constants, so they were modeled using double loops and double loops with Warburg tail circuits (see Fig. 8b, c). Those fitted models describe the steel/concrete interface as illustrated above. The obtained experimental data were analyzed using the Gamry Echem Analyst software version 5.3. This software used a non-linear least squares fitting algorithm to obtain the model parameters.

Nyquist diagrams for some beams are shown in Figs. 9 and 11, and the high frequency loops are shown in the upper-left corner in each figure. Bode diagrams are shown in Figs. 10 and 12. The spectra experimental data are shown as marker points and the fitted models are shown as lines. Figures 9 and 10 show the spectra for the beam G6-2 at cycle # 3, 6, and 9. The double loops with Warburg tail circuit model (Fig. 8c) was used to fit the experimental data with Warburg tail and obtained the model parameters. Also, the fitted model was sufficient good even at low frequency loop. Figures 11 and 12 show the spectra for the beam G9-2 at cycle # 3, 6, and 9. The double loops with Warburg tail circuit model was used to fit the experimental data for the cycle # 3 and 6 where diffusion control was appeared. However, at cycle # 9, the Warburg tail disappeared in the experimental data which required the circuit model to be double loops only without the Warburg tail in order to fit the data and obtain the model parameters.

Fig. 9 Nyquist plots for rebar in beam G6-2 at cycle # 3, 6, and 9. Fitted model results are shown

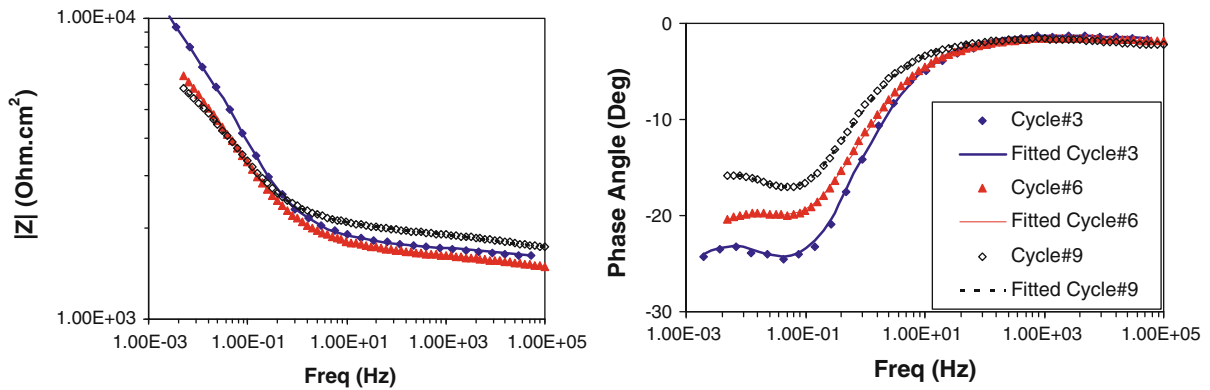
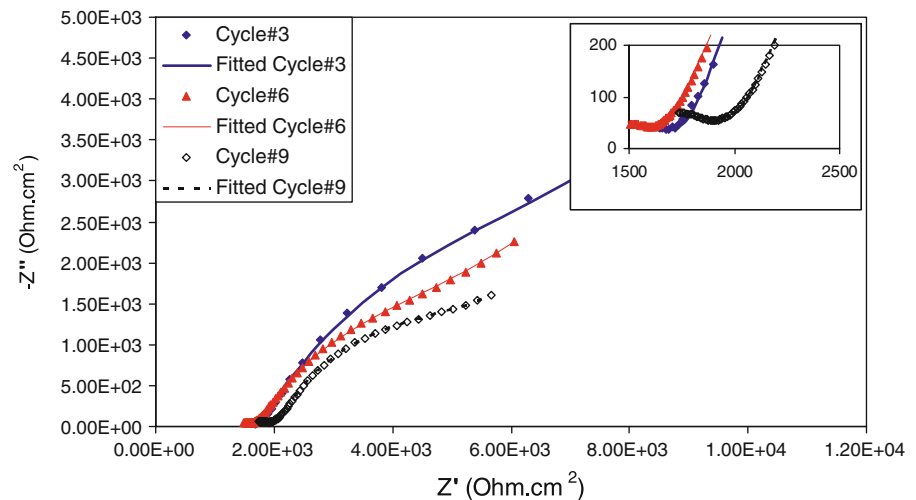


Fig. 10 Bode plots for rebar in beam G6-2 at cycle # 3, 6, and 9. Fitted model results are shown

The mass transfer effect (or effect of concentration polarization) appeared in G6 (Fig. 9), which is indicated by Warburg tail, was due to low oxygen availability near the rebar that had high corrosion activities. This was also validated by the present of black rust and high corrosion surface area of G6 as will be shown in the visual inspection next sections. On the other hand, the mass transfer effect (or effect of concentration polarization) appeared in G9 (Fig. 11), which is indicated by Warburg tail for cycle # 3 and 6, was due to high resistance of the passive film on the rebar which reduce the diffusion of oxygen to react with the substrate. Therefore, as the pitting initiated in the passive layer (as in cycle # 9 for G9-2), the Warburg tail disappeared. The similar trends appeared in G7 and G8, but the Warburg tail disappeared faster than G9. This result was validated with the visual inspection and chloride profile as will be seen next sections.

The phase angle that shown in Bode diagrams exceeds 65° in the passive condition (G9-2) and it reduces to around 40° as the pitting initiated. Also, as the corrosion activities increased and a uniform corrosion became dominate, the phase angle reaches to around 15° .

Figure 13 shows the average charge transfer resistance, R_{ct} , in log scale of the group G6–G9. The results obtained from the circuit modeling that fitted the experimental data. The resistance of G9 is improved with time due to the passive film formed around the rebar without any disturbance by ions chloride. The resistance of G9 is dropped suddenly at cycle # 9 which indicated to depassivation of the oxide film, and this is due that the chloride concentration reaches the threshold value of steel corrosion (see Sect. 4.5 below). Also, the resistance of G7 is better than G8. All these results are consistency with the previous results and have the same trends.

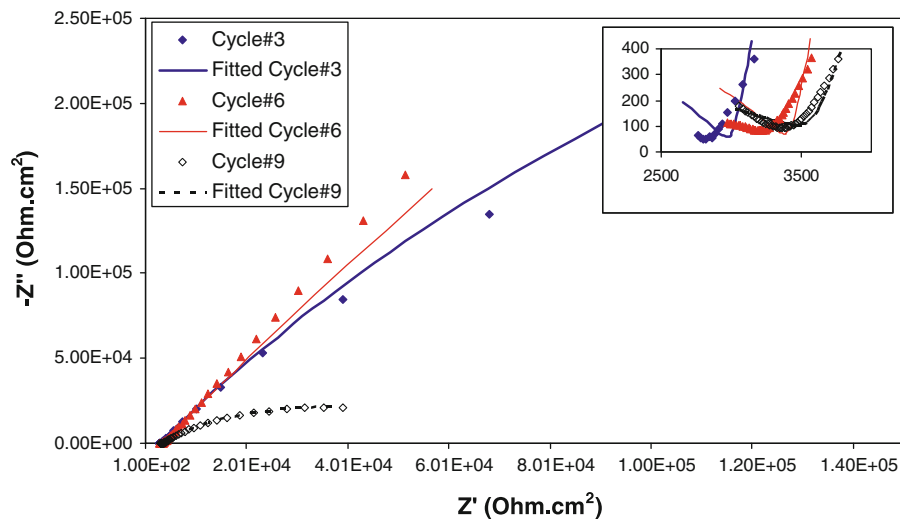


Fig. 11 Nyquist plots for rebar in beam G9-2 at cycle # 3, 6, and 9. Fitted model results are shown

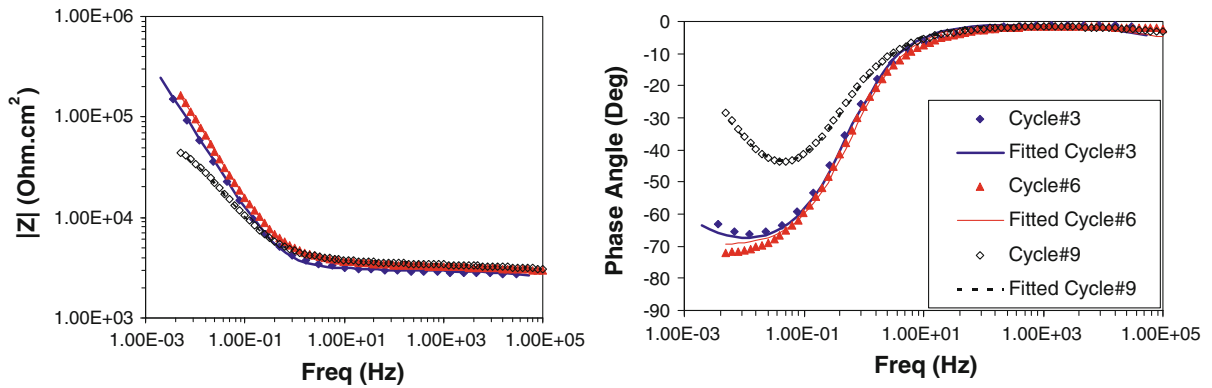


Fig. 12 Bode plots for rebar in beam G9-2 at cycle # 3, 6, and 9. Fitted model results are shown

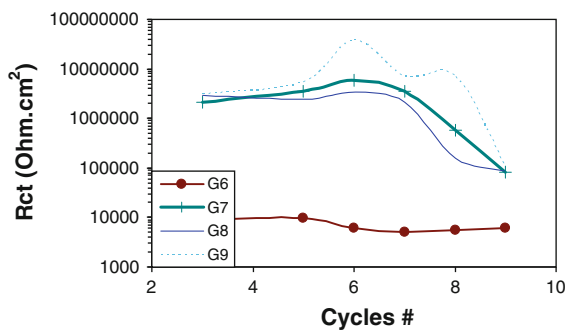


Fig. 13 Charge transfer resistance, Rct, results obtained from fitted circuit model for groups G6–G9

The slope of the $|Z|$ plot is another parameter that can be used to describe the spectra variation with time. Figure 14 shows how to construct the slope of $|Z|$ plot,

and it shown here for cycle # 9. In consequence of the slope decrease (in its absolute value), there is a decrease in the phase angle. Figure 15 shows the relation between charge transfer resistance and the slope of the $\log|Z|$ Bode plot for all groups in this study.

There is a correlation between the charge transfer resistance and the slope of the $\log|Z|$ Bode plot as seen in Fig. 15. This relation can be summarized as follows:

- if the slope $\sim < -0.6 \Rightarrow Rct > 1 \times 10^6 \text{ Ohm cm}^2$ (High resistance)
- if the slope between -0.6 to $-0.3 \Rightarrow 1 \times 10^4 < Rct < 1 \times 10^6 \text{ Ohm cm}^2$ (Medium resistance)
- if the slope $> -0.3 \Rightarrow Rct < 1 \times 10^4 \text{ Ohm cm}^2$ (Low resistance)



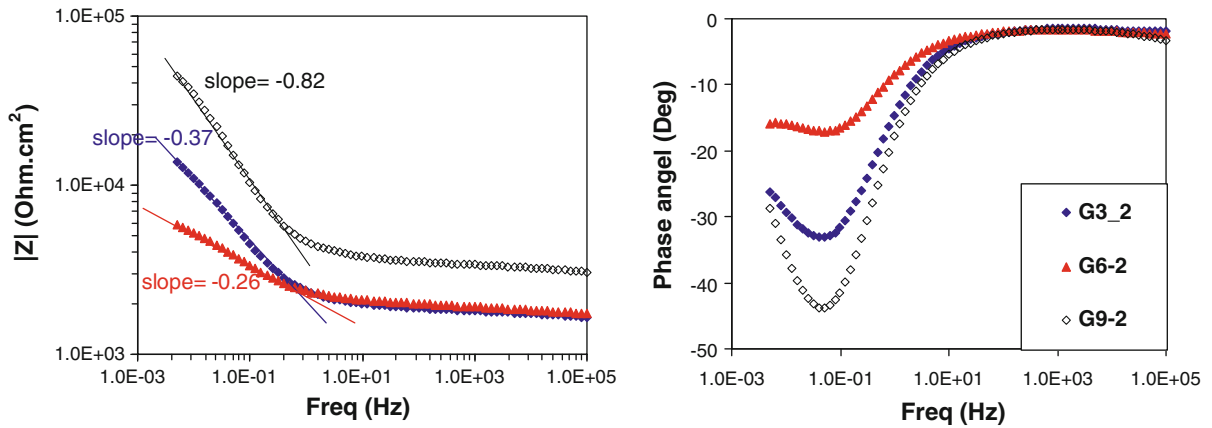


Fig. 14 Bode plots for cycle # 9 of beam G3-2, G6-2, G9-2, and shown the slope of the $|Z|$ plot

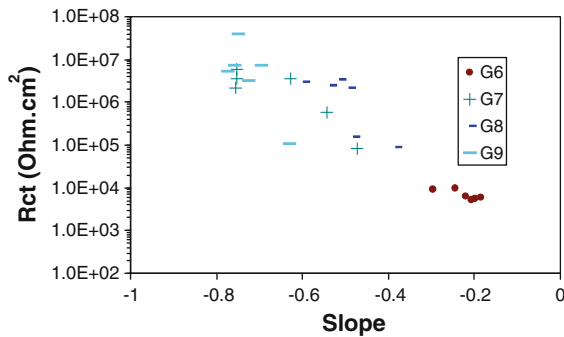


Fig. 15 Charge transfer resistance versus the slope of the $\log|Z|$ Bode plot

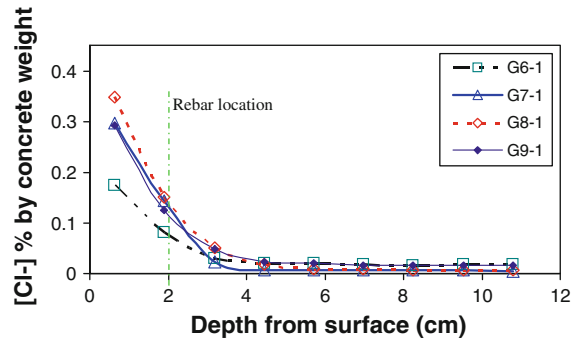


Fig. 16 Total chloride profiles versus the slab depth for specimen 1 of groups G6–G9

The above correlation ratios were similar to other works [25].

4.5 The chloride penetration profiles

The chloride penetration profiles of concrete specimens were obtained from one beam of each group when the corrosion potential of the beam transferred to high risk corrosion potential. This will allow distinguishing the profile at which the corrosion was accelerated in the rebar.

Figure 16 shows the total chloride profiles for groups G6–G9 at the beginning of high risk corrosion potential. The value of the chloride content at the top bars for G7-9 was around 0.15% by concrete weight, and it was half this value for G6. The high corrosion rate observed in G6 because the mechanical loading, which was 50% of ultimate strength, initiated a single crack in the beams, and the chloride ions flow through that crack and reached the top rebar directly

at the first cycle. Therefore, the mechanical loading (up to 50% of ultimate strength) did not effect the chloride diffusion in the concrete in general, and the concrete powder collection method gives the chloride content in a hole not at a single crack. This result goes with other researchers' results [30–32] who studied the effect of mechanical loading on transport properties. However, the localized crack that developed in the beams (at 50% loading) allowed the chloride ions to reach and depassivate the top rebar quickly. Therefore, the chloride content profile will not give any indication to corrosion activities when a mechanical loading was applied on the beam.

4.6 The visual inspections

The beams of group G6, which had pre-exposure loading up to 50% of ultimate capacity, had a major center crack developed beneath the application of the



load, and extended to the mid height of the beams. The maximum surface width of those cracks reaches up to 0.6 mm after load removed. On the other hand, no surface cracks observed on the surface for groups G7–G9, where no loading or 25% loading were applied.

The rebars were bringing out and observed from the beams after the concrete powder for the chloride profile test was collected. The corroded area in each rebar was estimated and the color of the corrosion products was recorded. Figure 17 shows the photos of beam rebars.

For the G6-1 beam, the top rebar had a uniform corroded area all over the rebar. The corroded area was around 94% of the total surface area. The corrosion color was reddish-brown and black color.

For the G8-1 beam, the top bar was corroded only at one small spot with area around 8% of the total surface area. The corrosion color was reddish-brown.

For the G7-1 and G9-1 beams, both top bars were corroded similar small spot with area around 4% of the total surface area. The corrosion color was reddish-brown.

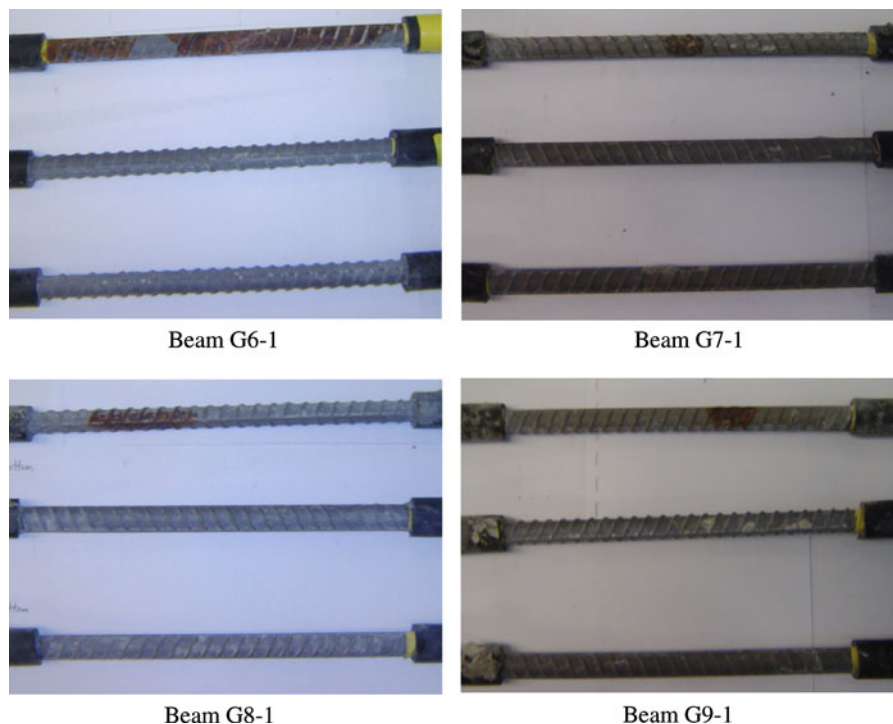
The formation of reddish-brown corrosion color indicated for the formation of ferrous ($\text{Fe}(\text{OH})_2$) and ferric hydroxide ($\text{Fe}(\text{OH})_3$) which formed where

excessive oxygen amount available. However, as the corrosion increases in the rebars, the black rust started to form on rebars (G6) which indicated for low oxygen availability for corrosion [7]. The comparison for the percent of corroded area among all beams showed similar trend as the macrocell corrosion currents.

5 Discussions

The results of the LPR, EIS, corrosion potential, and visual inspection are correlated, and this gives confidence for the results. Figure 18 shows the relation between the charge transfer resistance (from EIS) and the polarization resistance (from LPR). There is a strong correlation between both resistances among the whole range of resistance value, from high resistance at low corrosion activities to low resistance at high corrosion activities. This results behavior observed in other works [16, 33]. Also, Fig. 19 shows the correlation between the charge transfer and macrocell corrosion charge measured across the 100-Ohm resistance. There is good correlation between them. Also, as shown in the results, the agreement between the visual inspections and the

Fig. 17 Photos of beam rebars after the corrosion test arranged as top rebar is first and the bottom rebars are below



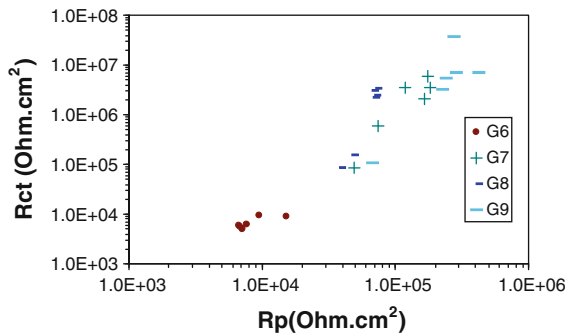


Fig. 18 Charge transfer resistance, R_{ct} , versus polarization resistance, R_p

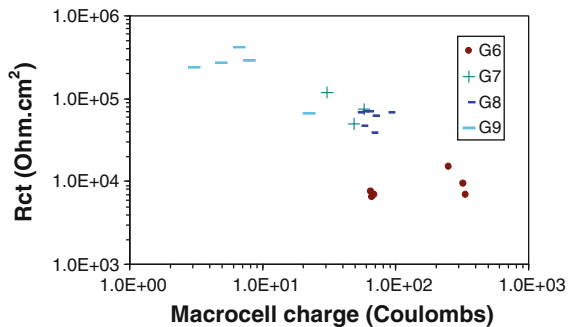


Fig. 19 Charge transfer resistance, R_{ct} , versus macrocell corrosion charge obtained from macrocell test results

electrochemical test results support the following discussion and conclusions.

5.1 Series (1) loading type effect

The loading for three-point bending (G7) and for four-point bending (G8) was up to 25% of the ultimate capacity, but the results showed that G8 had lower corrosion resistance, higher macrocell corrosion current, and higher corrosion rate as compared to G7. Also, the visual bars inspection showed similar results. The chloride profiles are similar for both groups (Fig. 16). The explanation for this is that, the maximum moment for three-point bending (G7) (shown in Fig. 1a) occurred only at a single section, whereas the maximum moment for four-point bending (G8) (shown in Fig. 1b) was constant between the two loads. Because the probability of having defects (like voids, local cracks, large aggregates, etc.) over a finite length is greater than at a single section, the formation of connected microcracks for G8 will be greater than G7 [15].

5.2 Series (2) loading value effect

The pre-exposure mechanical loading did not affect the chloride diffusion properties for the concrete where the chloride profiles are similar under different loadings as shown in Fig. 16. This results consistency with other works [30–32] with low level of applied load (less than 75%). Those previous research studied the diffusion properties on cylinder specimens where the load is equally distributed over the whole section. However, in this study the load applied on the beam where a single crack propagated beneath the application of the load (50% of the ultimate capacity), and extended to the mid height of the beams. This localized crack allowed the chloride ions to reach and depassivate the top rebar quickly. Therefore, the corrosion current for G6 was higher than G9.

The corrosion current obtained by macrocell or LPR for groups G7 and G9 are similar, and it indicated for low corrosion activities. Also, the corrosion potentials for both groups are not in the active zone. This confirmed that low level of loading (before continues cracks formed) does not effect the corrosion initiation. On the other hand, there is a large difference between the corrosion resistances of G7 and G9 (Fig. 6 for R_p , and Fig. 13 for R_{ct}). The polarization and charge resistances of G9 increased with time up to certain limits then a sudden decrease were observed at cycle # 9. The polarization and charge resistances of G7 did not show a similar improvement as G9. The continuous rising of G9 resistance can be explained by the growth of the passive layer around the rebar due to high alkalinity of intact concrete. This passive layer was destroyed suddenly when the chloride content reached critical value at cycle # 9. On the other hand, the application of mechanical load may induced a disturbance in the concrete-steel interfacial zone which reduce the growth of the passive layer around the rebar, thus no improvement was observed in the G7 polarization resistance. However, the high resistance of G9 did not delay the corrosion initiation, where at cycle # 9 both G7 and G9 showed similar resistance and corrosion potential (Figs. 5, 6, 13).

The passive layer formed on the rebars during the curing period for G6–G9, and it continued to enrichment in group G9 (where no load was applied) which indicated by the improvement in the polarization resistance. The application of the mechanical

loading after the curing period suppressed the growth of the passive layer and its resistance for both G7 and G8. However, the extra growth in the passive layer of G9 had no role on the corrosion initiation. In general, the pre-exposure mechanical load does not effect the concrete diffusion. Also, it has not influence on the corrosion initiation or corrosion rate thereafter, unless it reaches to some limit where it develops connected microcracks through which the chloride ions flow and depassivate the rebar. This results was shown in other works [7–10, 12].

6 Conclusions

The impact of the pre-exposure mechanical loading was studied and the following points can be concluded from this research:

1. The pre-exposure mechanical load (up to 50% of ultimate capacity) does not effect the concrete diffusion, and the chloride content profiles of the different load cases were similar. The impact of the load on the steel corrosion was localized where a visible continuous crack formed.
2. The pre-exposure mechanical load has not influence on the corrosion initiation or corrosion rate thereafter, unless it reaches to some limit where it develops connected cracks through which the chloride ions flow and depassivate the rebar.
3. The 25% of the ultimate capacity load seems to be at the critical limit where some microcracks onset to be connected and facilitate the chloride ions flow.
4. The passive layer formed on the rebars during the curing period, and it continued to enrichment (if no load was applied) which indicated by the improvement in the polarization resistance. However, the application of the mechanical loading after the curing period suppressed the growth of the passive layer and its resistance.
5. The range of corrosion resistance of the rebar can be classified according to the slope and phase angle of the Bode diagrams. Also, corrosion of steel reinforcement in concrete can be monitored using EIS test, and this test is able to distinguish the different stages of corrosion, e.g., passive, initiation, and growth of corrosion.

References

1. Cabrera JG (1996) Deterioration of concrete due to reinforcement steel corrosion. *Cem Concr Compos* 18(1): 47–59
2. Huang R, Yang CC (1997) Condition assessment of reinforced concrete beams relative to reinforcement corrosion. *Cem Concr Compos* 19(2):131–137
3. Sherwood EG, Soudki KA (2000) Rehabilitation of corrosion damaged concrete beams with CFRP laminates—a pilot study. *Compos B Eng* 31(6–7):453–459
4. Fang C, Gylltoft K, Lundgren K, Plos M (2006) Effect of corrosion on bond in reinforced concrete under cyclic loading. *Cem Concr Res* 36(3):548–555
5. Mangat PS, Elgarf MS (1999) Strength and serviceability of repaired reinforced concrete beams undergoing reinforcement corrosion. *Mag Concr Res* 51(2):97–112
6. Castel A, Francois R, Arliguie G (2006) Mechanical behaviour of corroded reinforced concrete beams—Part 1: experimental study of corroded beams. *Mater Struct* 33(9): 539–544
7. Bentur A, Diamond S, Berke NS (1997) *Steel corrosion in concrete*, 1st edn. E & FN Spon, London
8. Li CQ (2000) Corrosion initiation of reinforcing steel in concrete under natural salt spray and service loading—results and analysis. *ACI Mater J* 97(6):690–697
9. Jacobsen S, Marchand J, Gerard B (1998) Concrete cracks I: durability and self healing—a review. In: Gjorv OE, Sakai K, Banthia N (eds) *The second international conference on concrete under severe conditions*. E & FN Spon, Tromsø, pp 217–231
10. Francois R, Arliguie G, Castel A (1998) Influence of service cracking on service life of reinforced concrete. In: Gjorv OE, Sakai K, Banthia N (eds) *The second international conference on concrete under severe conditions*. E & FN Spon, Tromsø, pp 143–152
11. Castel A, Francois R, Arliguie G (1999) Effect of loading on carbonation penetration in reinforced concrete elements. *Cem Concr Res* 29(4):561–565
12. Francois R, Maso JC (1988) Effect of damage in reinforced concrete on carbonation or chloride penetration. *Cem Concr Res* 18(6):961–970
13. Yoon S, Wang K, Weiss WJ, Shah SP (2000) Interaction between loading, corrosion, and serviceability of reinforced concrete. *ACI Mater J* 97(6):637–644
14. Kondratova IL, Montes P, Bremner TW (2003) Natural marine exposure results for reinforced concrete slabs with corrosion inhibitors. *Cem Concr Compos* 25(4–5):483–490
15. Ersoy U, Ozecebe G, Tankut T (2003) *Reinforced concrete*, 2nd edn. Middle East Technical University, Ankara
16. Jones DA (1996) *Principles and prevention of corrosion*, 2nd edn. Prentice-Hall, Inc., Upper Saddle River
17. Bertolini L, Elsense B, Pedferri P, Polder R (2004) *Corrosion of steel in concrete: prevention, diagnosis, repair*. Wiley-VCH Verlag GmbH & Co. KGaA, Weinheim
18. Ababneh A (2002) The coupled effect of moisture diffusion chloride penetration and freezing-thawing on concrete durability. PhD Dissertation, University of Colorado
19. Gonzalez JA, Andrade C (1982) Effect of carbonation, chloride and relative ambient humidity on the corrosion of

- galvanized rebars embedded in concrete. *Br Corros J* 17(1):21–28
20. Morris W, Vazquez M, De Sanchez SR (2000) Efficiency of coatings applied on rebars in concrete. *J Mater Sci* 35:1885–1890
 21. Darwin D, Browning JP, Nguyen T, Locke CE (2002) Mechanical and corrosion properties of a high-strength, high chromium reinforcing steel for concrete. Rep. No. SD2001-05-F. South Dakota Department of Transportation Office of Research, Federal Highway Administration, U.S. Department of Transportation, Lawrence
 22. Dhouiabi L, Triki E, Raharinaivo A, Trabanelli G, Zucchi F (2000) Electrochemical methods for evaluating inhibitors of steel corrosion in concrete. *Br Corros J* 35(2):145–149
 23. Kendig M, Scully JR (1990) Basic aspects of electrochemical impedance application for the life prediction of organic coating on metals. *Corrosion* 46(1):22–29
 24. Monticelli C, Frignani A, Trabanelli G (2002) Corrosion inhibition of steel in chloride-containing alkaline solutions. *J Appl Electrochem* 32(5):527–535
 25. Montemor MF, Simoes AMP, Salta MM (2000) Effect of fly ash on concrete reinforcement corrosion studied by EIS. *Cem Concr Compos* 22:175–185
 26. Hachani L, Carpio J, Fiaud C, Raharinaivo A, Triki E (1992) Steel corrosion in concrete deteriorated by chlorides and sulphates: electrochemical study using impedance spectrometry and “stepping down the current” method. *Cem Concr Res* 22:56–66
 27. Jianguo L, Gaoping G, Chuanwei Y (2005) EIS study of corrosion behaviour of organic coating/Dacromet composite systems. *Electrochim Acta* 50(16–17):3320–3332
 28. Buchheit RG, Cunningham M, Jensen H, Kendig M, Martinez MA (1998) A correlation between salt spray and electrochemical impedance spectroscopy test results for conversion-coated aluminum alloys. *Corrosion* 54(1): 61–72
 29. Chen H, Wheat HG (1996) Evaluation of selected epoxy-coated reinforcing. In: *Corrosion 96, the NACE international annual conference and exposition*
 30. Hearn N (1999) Effect of shrinkage and load-induced cracking on water permeability of concrete. *ACI Mater J* 96(2):234–241
 31. Samaha H, Hover KC (1992) Influence of microcracking on the mass transport properties of concrete. *ACI Mater J* 89(4):416–424
 32. Yang Z, Weiss WJ, Olek J (2006) Water transport in concrete damaged by tensile loading and freeze-thaw cycling. *Construct Build Mater* 18(3):424–434
 33. Benjamin MM, Sontheimer H, Leroy P (1996) Corrosion of iron and steel. In: *Internal corrosion of water distribution systems*. American Water Works Association Research Foundation and DVGW, Denver, pp 29–70